Three-dimensional transient and harmonic shear-wave scattering by a soft cylinder for dynamic vascular elastography

Anis Hadj Henni[a),b)]
Laboratory of Biorheology and Medical Ultrasonics, University of Montreal Hospital Research Center, Montreal, QC H2L 2W5, Canada

Cédric Schmitt
Laboratory of Biorheology and Medical Ultrasonics, University of Montreal Hospital Research Center, Montreal, QC H2L 2W5, Canada and Institute of Biomedical Engineering, University of Montreal, Montreal, QC H3C 3J7, Canada

Guy Cloutier[a),c)]
Laboratory of Biorheology and Medical Ultrasonics, University of Montreal Hospital Research Center, Montreal, QC H2L 2W5, Canada; Institute of Biomedical Engineering, University of Montreal, Montreal, QC H3C 3J7, Canada; and Department of Radiology, Radio-Oncology and Nuclear Medicine, University of Montreal, Montreal, QC H3T 1J4, Canada

(Received 17 April 2008; revised 18 July 2008; accepted 19 July 2008)

With the objective of characterizing biological soft tissues with dynamic elastography, a three-dimensional (3D) analytical model is proposed to simulate the scattering of plane shear waves by a soft cylinder embedded in an infinite soft medium. The 3D problem of harmonic plane shear-wave scattering is first formulated and solved, and the monochromatic solution is employed to simulate transient wave scattering. Both harmonic and transient simulations are compared with experimental 3D acquisitions. The good agreements obtained between measured and calculated displacement fields allowed to conclude on the validity of the proposed 3D harmonic and transient models. The spatial distribution of displacements (diffraction lobes, displacement oscillations, wave diffraction angles, etc.) and their relative amplitudes in both inclusion and surrounding materials depended on the contrast between the viscoelastic properties of the different media. The possibility of solving an inverse problem to assess soft heterogeneous medium viscoelasticity is discussed and some future theoretical and experimental developments are proposed.
© *2008 Acoustical Society of America.* [DOI: 10.1121/1.2973194]

PACS number(s): 43.80.Qf, 43.80.Vj, 43.80.Ev, 43.35.Mr [FD] Pages: 2394–2405

I. INTRODUCTION

Detection and characterization of vascular pathologies are of great importance since they are responsible for more than one-third of global deaths caused by cardiovascular diseases in the world[1] (2002 World Health Organization statistics). In this context, the present work is dedicated to study, theoretically and experimentally, shear-wave (SW) scattering by mimicked venous thrombi[2] in order to enrich existing diagnostic methods, such as ultrasound imaging, x-ray angiography, and magnetic resonance imaging (MRI), by a new one based on dynamic elastography. Indeed, it has been proven that viscoelastic properties of coagulated blood depend on the clot age and composition.[3–5] This dependence is currently exploited to perform qualitative static elastography imaging (using a static or quasistatic loading to image the strain distribution in the medium)[6,7] but this technique is sensitive to mechanical boundary conditions and motion artifacts and does not allow to measure tissue viscosity. However, quantitative elasticity and viscosity imaging could become an interesting clinical indicator for pathology diagnosis and therapy planning.

Contrary to static methods, dynamic elastography[8,9] permits to perform viscoelastic characterization of living tissues by studying traveling of elastic SWs into the probed medium. Since SW speeds in soft tissues are very low (few meters per second) compared to compression waves, it is possible to track them with an ultrafast ultrasonic imaging system that can typically produce more than 5000 images per second. Compared to static methods, SW tracking allows to determine their velocity and attenuation independently of the mechanical boundary conditions. Moreover, the fast imaging system is not sensitive to typical motion artifacts since the propagation occurs during few milliseconds. Dynamic elastography allows to obtain the spatiotemporal displacement evolution and, consequently, the wave-medium interaction to perform tissue mechanical characterization. Here, one has to notice that contrary to elastic waves in solids, the total displacement field in tissues can be experimentally measured and imaged.

[a)]Authors to whom correspondence should be addressed.
[b)]Electronic mail: anis.hadjhenni@crchum.qc.ca
[c)]Electronic mail: guy.cloutier@umontreal.ca

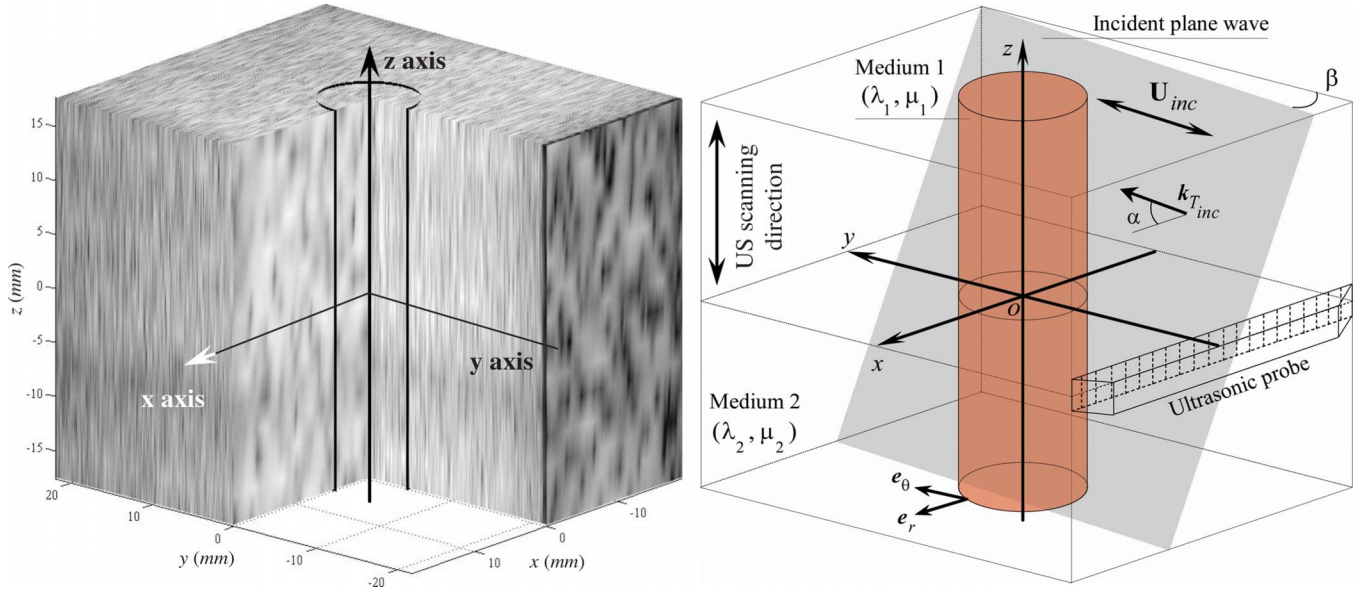

FIG. 1. (Color online) Left: 3D view of the reconstructed B-mode ultrasonic image of the experimentally tested heterogeneous medium. There is no echogenicity contrast between the agar-gelatin cylindrical inclusion (represented in the image) and its surrounding soft medium. Right: 3D representation of the plane SW scattering problem. The incident plane wave makes an angle of α with its propagation direction and is inclined in the plane $(o,\boldsymbol{e}_x,\boldsymbol{e}_y)$ from the y axis by an angle β.

A. Dynamic elastography in medicine

The first applications of SW imaging in bioacoustics were performed using M-mode ultrasonography[10] and Doppler for sonoelasticity,[11,12] MRI for magnetic resonance elastography,[13] or by means of real-time ultrafast ultrasonic imaging for both harmonic and transient elastographies.[14,15] Concerning transient elastography, most of modeling works concerned analytical or numerical simulation of SW generation obtained by impact methods[15] or by ultrasound radiation forces.[16,17] The interaction of SWs with confined heterogeneities in inhomogeneous tissues has not yet been precisely modeled despite the fact that to characterize mechanically many pathologies such as clotted vessels, tumors, etc., it is necessary to simulate and understand SW scattering by such inhomogeneities.

B. Objectives

An application of dynamic elastography to venous and arterial pathologies is presented here. The aim was to model analytically and to study, theoretically and experimentally, SW scattering by a venous clot, modeled by a cylindrical soft inclusion surrounded by an infinite soft medium. From a mechanical point of view, both inclusion and surrounding media were assumed to be made of homogeneous, isotropic, and linear viscoelastic materials.

A three-dimensional (3D) analytical model was developed to simulate the scattering of a harmonic plane SW by a cylindrical inclusion for an arbitrary incident angle. Following theoretical works of Faran,[18] White,[19] Fan *et al.*,[20] and Honarvar and Sinclair[21] on scattering of plane waves by cylindrical solids, the solution was formulated using a modal decomposition technique. The superposition principle of harmonic solutions (stationary displacement fields) served to obtain the 3D scattered field for an arbitrary incident transient plane SW. It is important to note that the model proposed in the present work can be coupled with magnetic resonance elastography or sonoelastography techniques.

Before validating experimentally the 3D model, the image acquisition process and the experimental setup that were used to produce ultrafast scanning are first described. The experimental material was composed of an agar-gelatin phantom (tissue mimicking material) containing a soft cylindrical inclusion, which simulated a venous clot. Both theoretical and experimental results are compared and discussed to investigate the validity of simulations. In the light of this discussion, a set of future possible applications and perspectives is presented, in particular, to solve the inverse problem allowing to characterize blood clot mechanical properties.

II. THEORY

To introduce the model, Fig. 1 shows a B-mode ultrasonic image of the 3D volume experimentally probed. The imaged soft agar-gelatin volume contained a circular cylindrical inclusion made of a mechanically different agar-gelatin material. One can observe that there is no echogenicity contrast between the inclusion and its surrounding medium despite their viscoelasticity differences. It will be shown (in Sec. IV) that a strong mechanical contrast appears between these two media when a SW propagates and interacts with the inclusion.

A. Problem formulation

The inclusion (blood clot phantom) was assumed to be a circular cylinder, of radius R, made of a soft material (medium 1) and surrounded by an infinite soft tissue (medium 2). Both media were assumed to be homogeneous, isotropic, linear, and viscoelastic. It is known that, for a certain frequency range (namely, for a few hundred hertz), the mechanical behavior of the agar-gelatin material is governed by the Hooke–Voigt viscoelastic behavior law.[22] This is in agree-

ment with a preliminary experimental work[23] that also suggested that coagulated blood viscoelasticity follows the same Hooke–Voigt model. This latter relies on the frequency domain, the stress, $\boldsymbol{\sigma}$, and the strain, $\boldsymbol{\varepsilon}$, tensors in the following way:

$$\boldsymbol{\sigma} = (\mathbf{C}' + i\omega\mathbf{C}'')\boldsymbol{\varepsilon}, \tag{1}$$

where $\mathbf{C}'$ and $\mathbf{C}''$ are the stiffness and viscosity tensors, respectively. For an isotropic and viscoelastic material, the complex stiffness tensor, $\mathbf{C}=\mathbf{C}'+i\omega\mathbf{C}''$, depends on the complex Lamé coefficients λ and μ. According to this, and in order to easily take into account the viscosity, the elastodynamic problem was expressed in the frequency domain. Since studied materials are soft, the bulk moduli λ of both media are not significantly different and were chosen to ensure a compression wave speed equal to 1540 m/s (ultrasound speed in biological tissues) for tissue densities of 1100 $\mathrm{kg/m^3}$. Consequently, scattering of SWs in such materials depends strongly on the complex shear moduli.

The problem geometry, given in Fig. 1, was described in a Cartesian system of coordinates $(o,\boldsymbol{e}_x,\boldsymbol{e}_y,\boldsymbol{e}_z)$ but regarding the cylinder circular geometry and to simplify the expression of mechanical boundary conditions, the elastodynamic problem was expressed and solved in a cylindrical system of coordinates $(o,\boldsymbol{e}_r,\boldsymbol{e}_\theta,\boldsymbol{e}_z)$. The inclined incident plane SW, represented in Fig. 1, propagates with an incidence angle α, formed by the incident shear wavevector $\boldsymbol{k}_{T_{\mathrm{inc}}}$ and the polarization plane $(o,\boldsymbol{e}_x,\boldsymbol{e}_y)$. Finally, and for more generality, the incident wave polarization, $\mathbf{U}_{\mathrm{inc}}$ contained in the plane $(o,\boldsymbol{e}_x,\boldsymbol{e}_y)$, was doing an angle β with the y axis, see Fig. 1.

From these geometrical considerations, one can conclude that the scattering problem is 3D and that mode conversions of SWs can occur. Consequently, diffracted waves were expressed as a combination of compression and SWs in both media. The incident plane SW was first considered to be harmonic with an angular frequency ω. Then, the harmonic solution was derived to model the scattering of arbitrary transient plane SWs.

B. The stationary problem

In the following, the subscript 1 is assigned to the cylinder constitutive material, whereas the subscript 2 designates the surrounding medium. In addition, the longitudinal (compression) and transverse (shear) wavevectors in the medium j ($j=\{1,2\}$) are labeled by $\boldsymbol{K}_j$ and $\boldsymbol{k}_j$, respectively. Both of these wavevectors are decomposed into components parallel to the z axis, called $K_{j_z}=K_j \sin\alpha$ and $k_{j_z}=k_j \sin\alpha$, and other ones contained in the plane $(o,\boldsymbol{e}_r,\boldsymbol{e}_\theta)$ (perpendicular to the cylinder axis) given by $K_{j_\perp}=K_j\cos\alpha$ and $k_{j_\perp}=k_j\cos\alpha$.

The displacement field in both media satisfies the Navier elastodynamic wave equation.[24] Applying a Fourier transform to this equation, one obtains

$$\rho_j\omega^2\mathbf{U}_j + (\lambda_j + 2\mu_j)\,\boldsymbol{\nabla}(\boldsymbol{\nabla}\cdot\mathbf{U}_j) - \mu_j\,\boldsymbol{\nabla}\times(\boldsymbol{\nabla}\times\mathbf{U}_j) = \mathbf{0} \quad \text{with} \quad j=\{1,2\}, \tag{2}$$

where $\mathbf{U}_j=(U_{r_j}\ U_{\theta_j}\ U_{z_j})^T$ is the displacement field in a phase $j=\{1,2\}$, ρ_j is the density, and λ_j and μ_j are the complex viscoelastic Lamé coefficients. The Helmholtz decomposition technique permits to express the displacement field in both media into scalar and vector potentials:[25]

$$\mathbf{U}_j = \boldsymbol{\nabla}\varphi_j + \boldsymbol{\nabla}\times(\psi_j\boldsymbol{e}_z) + R\,\boldsymbol{\nabla}\times\boldsymbol{\nabla}\times(\chi_j\boldsymbol{e}_z) \quad \text{with} \quad j=\{1,2\}. \tag{3}$$

Mechanically, $\varphi_j(r,\theta)$ is the displacement scalar potential associated with compression waves in phase j and $\psi_j\boldsymbol{e}_z$ and $\chi_j\boldsymbol{e}_z$ are the vector potentials of displacements polarized following the $(o,\boldsymbol{e}_r,\boldsymbol{e}_\theta)$ plane and another parallel to the z axis, respectively. Each of these potentials satisfies the well known Helmholtz wave equation.

Following the classical modal decomposition method, these potentials can be expressed as infinite series of Bessel and angular functions containing unknown coefficients, except for the known incident purely SW contained in the plane $(o,\boldsymbol{e}_r,\boldsymbol{e}_\theta)$. This latter depends only on the vector potential ψ_{inc} ($\mathbf{U}_{\mathrm{inc}}=\boldsymbol{\nabla}\times\psi_{\mathrm{inc}}\boldsymbol{e}_z$). Consequently, we can choose to express the shear incident field by its potential, which is written in a cylindrical system of coordinates as[18–21]

$$\psi_{\mathrm{inc}} = \mathrm{amp}(\omega)\sum_{n=0}^{+\infty}\frac{1}{\psi_0}\varepsilon_n(i)^n J_n(k_{2_\perp}r)\times\cos(n(\theta-\beta))e^{(ik_{2_z}z-i\omega t)}, \tag{4}$$

where ε_n is the Neumann factor, i.e., $\varepsilon_0=1$ and $\varepsilon_n=2$ for $n\geq 1$. One has to note that the incident wave's inclination angle β, in the plane $(o,\boldsymbol{e}_r,\boldsymbol{e}_\theta)$, acts like a rotation angle applied to the wave corresponding to $\beta=0$ (i.e., an incident wave propagating following the x axis). The incident wave amplitude, $\mathrm{amp}(\omega)$, is fixed to 1 for harmonic incident waves and is equal to the excitation amplitude (complex amplitude) in the case of a transient incident wave (see Sec. II C). The normalization coefficient, ψ_0, ensures that the maximum amplitude of the incident harmonic wave is equal to unity regardless of the frequency.

In a similar way, transmitted and reflected displacement fields can be expressed via their potentials. Considering the fact that the displacement at the cylinder center is finite, only the first kind Bessel functions $J_n(\cdot)$ serve to express the refracted potentials. The three displacement potentials within the inclusion are then given by

$$\varphi_1 = \sum_{n=0}^{+\infty} A_n J_n(K_1 r)\sin(n(\theta-\beta))e^{ik_{2_z}z},$$

$$\psi_1 = \sum_{n=0}^{+\infty} B_n J_n(k_1 r)\cos(n(\theta-\beta))e^{ik_{2_z}z},$$

$$\chi_1 = \sum_{n=0}^{+\infty} C_n J_n(k_1 r)\sin(n(\theta-\beta))e^{ik_{2_z}z}. \tag{5}$$

In these expressions and in the following, the harmonic time dependence term is omitted for simplification.

The displacement potentials in the surrounding medium are composed of those of the incident plane wave Eq. (4) and of the scattered ones. Knowing that scattered waves are out-

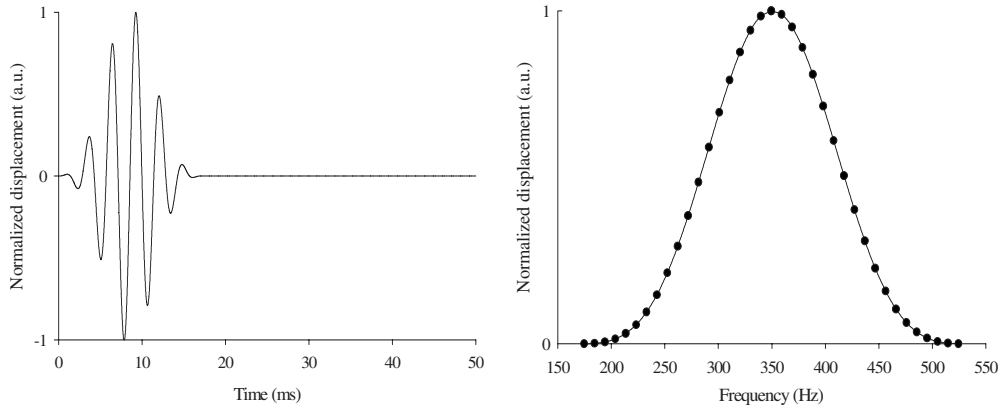

FIG. 2. Left: incident transient wave temporal form used in experiments and simulations. The wave is composed of six modulated pulses with 350 Hz central frequency. Right: the discretized incident wave spectrum representing the calculation points (●).

going, they are expressed by means of first kind Hankel functions $H_n^{(1)}(\cdot)$. One finally obtains the following scattered potential expressions:

$$\varphi_2 = \sum_{n=0}^{+\infty} D_n H_n^{(1)}(K_{2_\perp} r)\sin(n(\theta-\beta))e^{ik_{2_z}z},$$

$$\psi_2 = \sum_{n=0}^{+\infty} E_n H_n^{(1)}(k_{2_\perp} r)\cos(n(\theta-\beta))e^{ik_{2_z}z},$$

$$\chi_2 = \sum_{n=0}^{+\infty} F_n H_n^{(1)}(k_{2_\perp} r)\sin(n(\theta-\beta))e^{ik_{2_z}z}. \quad (6)$$

One can note that the axial wave number k_{2_z} is the same in both media. It has to be equal to the axial component of the incident SW since stress and displacements are continuous at the cylinder interface. Moreover, it is important to note that the angular dependencies in Eqs. (5) and (6) were chosen to be in agreement with the symmetry and antisymmetry properties of the different elastic waves (i.e., the incident and the scattered ones).[19]

At the cylinder boundary, the continuity of displacements and normal stress (given by $\boldsymbol{\sigma}\cdot\boldsymbol{n}$, where $\boldsymbol{\sigma}$ is the stress matrix and $\boldsymbol{n}$ is the unit vector normal to the cylinder) permits to determine the unknown coefficients A_n, B_n, C_n, D_n, E_n, and F_n in Eqs. (5) and (6). These conditions are summarized as follows:

$$\begin{aligned}&(U_{r1}\ \ U_{\theta 1}\ \ U_{z1})^T = (U_{r2}\ \ U_{\theta 2}\ \ U_{z2})^T\\ &(\sigma_{rr1}\ \ \sigma_{r\theta 1}\ \ \sigma_{rz1})^T = (\sigma_{rr2}\ \ \sigma_{r\theta 2}\ \ \sigma_{rz2})^T \quad \text{at} \quad r\\ &\quad = R \ \text{ and } \ \theta \in [0,2\pi].\end{aligned} \quad (7)$$

Using Eqs. (1) and (3), displacement and stress fields expressed at $r=R$ in Eq. (7) can be written with respect to potentials given in Eqs. (5) and (6). The orthogonality property of angular functions over the interval $[0,2\pi]$ allows to separate the boundary conditions in Eq. (7) into an infinite set of equations with respect to the infinite series orders n $(n=0,\ldots,+\infty)$. For a given mode of order n, it appears, after calculations, that the unknown coefficients A_n, B_n, C_n, D_n, E_n, and F_n are related to a set of known terms, which depend on the incident SW, by means of a linear system of equations:

$$T_n(A_n\ \ B_n\ \ C_n\ \ D_n\ \ E_n\ \ F_n)^T = \mathbf{b}_n \quad \text{with} \quad r=R \ \text{ and } \ n = 0,\ldots,+\infty. \quad (8)$$

In Eq. (8), the (6×6) T_n matrix depends on the geometry and the mechanical properties of media 1 and 2, while the second member $\mathbf{b}_n$ represents the incident wave contribution to the nth displacement and stress terms, expressed at the cylinder boundary. Both $\mathbf{T}_n$ and $\mathbf{b}_n$ elements are detailed in the Appendix. Solving the system of Eq. (8), by using a classical matrix inversion algorithm[26] to avoid fastidious calculations using the Cramer rule (which formulates solutions explicitly), provides for each integer order n the searched coefficients. These latter permit then to calculate the total stationary displacement field by means of expressions (4)–(6) and (3). Since one cannot calculate all terms of the infinite series appearing in the displacement field expression, the maximum calculation order is limited to a finite order. The truncation order, which depends on the inclusion size and on the incident wave frequency, was fixed for the simulations presented here to 50 terms.

C. Transient-wave scattering

Following the superposition principle in the spectral domain,[24] transient SW scattering by a homogeneous soft circular cylinder was modeled using the previous harmonic wave scattering model. Indeed, any incident wave, having an arbitrary temporal profile, can be expressed in the frequency domain by means of a temporal Fourier transform. In practice, the relevant frequencies are frequently limited to a certain interval with no significant information outside it (see the example in Fig. 2). Consequently, by choosing to express the transient wave scattering problem in the frequency domain, one can discretize the frequency range of interest into a finite number of calculation points (Fig. 2) and solve, for each frequency-wave amplitude couple $(\omega,\text{amp}(\omega))$ in Eq. (4), the associated harmonic problem using the model previously presented. This set of stationary solutions provides the diffracted transient wave spectrum. The temporal diffracted field was finally obtained from the spectral solution by

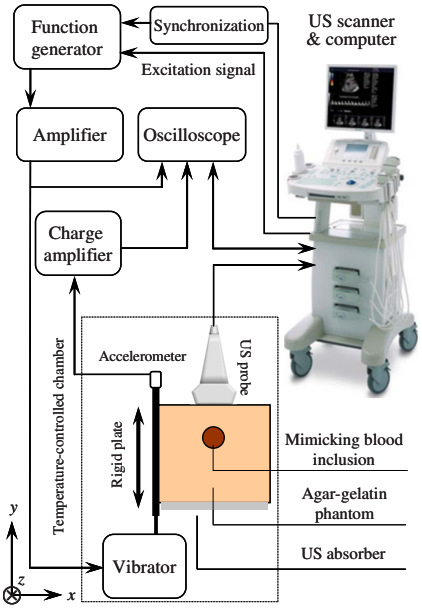

FIG. 3. (Color online) A schematic representation of the experimental setup: the SW generation and the ultrasonic acquisition devices.

means of an inverse Fourier transform. Compared to a temporal solving strategy, this spectral method is faster and permits to model more easily viscoelastic effects (since temporal convolution products appearing when viscosity is modeled are transformed into simple products in the frequency domain).

III. EXPERIMENTAL SETUP

A. Generation of shear waves and ultrafast acquisition system

In the experimental setup schematized in Fig. 3, SWs were generated by a large rigid plate (202×85 mm^2) attached to a vibrator (type 4810, Brüel&Kjær, Nærum, Denmark) and applied on the phantom surface. The low frequency harmonic or transient vibration was produced with a function generator (model 33250A, Agilent, Palo Alto, CA), amplified (type 2706, low frequency amplifier, Brüel&Kjær) before supplying the minishaker. In this configuration, the propagation direction of the plane SWs was orthogonal to the plate motion. A clinical array transducer (model L14-5/38, 38 mm width, 128 elements, Ultrasonix) connected to the Sonix RP scanner (Ultrasonix Medical Corporation, Burnaby, BC, Canada) was positioned parallel to the tissue motion to acquire and reconstruct radio-frequency (RF) sequences at a high frame rate (3850 Hz). The ultrafast imaging method used here was inspired from an electrocardiogram-gated image acquisition strategy to reach high frame rates.[27,28] In the present case, synchronization was achieved using SW gating by considering the starting of the mechanical excitation.

The probe excitation frequency, the sampling frequency, and the bit depth were 10 MHz, 40 MHz, and 16 bits, respectively. To avoid reverberation artifacts, an acoustical absorber was placed on the front of the probe. The true plate motion was acquired with an accelerometer (type 4375, Brüel&Kjær) connected to a charge amplifier (type 2692, Nexus Amplifier, Brüel&Kjær). The part of the experimental setup including the phantom was enclosed in a temperature-controlled chamber regulated at 20 °C.

The agar-gelatin phantom was made following a protocol described in a previous work.[29] The surrounding material was made (in proportion of the water weight) of 4.0% porcine skin gelatin and 3.0% agar powder (product No. G-1890 for gelatin and No. A-9799 for agar, Sigma Chemical, St. Louis, MO) and contained an agar-gelatin cylindrical inclusion composed of 2.5% porcine skin gelatin and 1.0% agar. The whole phantom had a parallelepipedal geometry ($20.5 \times 27.5 \times 10.5$ cm^3) and the inclusion was a 9.8 mm diameter cylinder. This latter formed an angle of $\alpha = 46°$ (i.e., the incidence angle) with the moving plate (positioned vertically) and had a length equal to 15.5 cm.

To image the 3D displacement field, RF ultrasonic signals at 14 consecutive planes (38.0×40.0 mm^2) were acquired every 2.5 mm along the z axis (for a 35.0 mm scanning distance) by adjusting automatically the probe position with a positioning step motor. A normalized cross-correlation algorithm applied to the acquired RF signals allowed to obtain the y displacement field component and its temporal evolution for the different slices. Finally, the 3D displacement field was reconstructed by superposing, along the z axis, the two-dimensional (2D) consecutive measured fields. In what follows, one has to note that both experimental and simulated displacement fields [in 3D, 2D and one-dimensional (1D) representations] have been normalized by their respective maximum displacement value.

B. Viscoelasticity of phantom components

Since mechanical properties have to be entered into the model to calculate displacement fields and in order to validate simulations, i.e., to solve the forward problem, it was necessary to assess viscoelastic properties of the gel materials that were used. The viscoelastic properties of phantom materials were determined by using 2D dynamic elastography[22] based on our ultrafast imaging system. Using this approach, the viscoelasticity was obtained by solving an inverse problem[22] based on the phase velocity and attenuation of plane SWs propagating in a homogeneous gel sample. A multifrequency study (using harmonic plane waves at different frequencies) allowed to assess the Hooke–Voigt viscoelastic parameters.

The two agar-gelatin materials (surrounding medium and inclusion) were characterized by using a separate homogeneous and parallelepipedal phantom for each of them. Viscoelastic properties were assessed between 50 and 440 Hz for the surrounding material and from 50 to 360 Hz for the inclusion material. Since this latter was very soft and viscous, high frequency plane SWs did not propagate sufficiently to characterize the inclusion material at frequencies above 360 Hz (as it can be shown by simulation, such a problem is avoided when the soft material is confined, for example, in a cylindrical form into a harder one). The experimental viscoelastic mean values and relative errors (i.e., the ratio between the standard deviation and the mean value) for the two samples were obtained by assessing plane SW veloc-

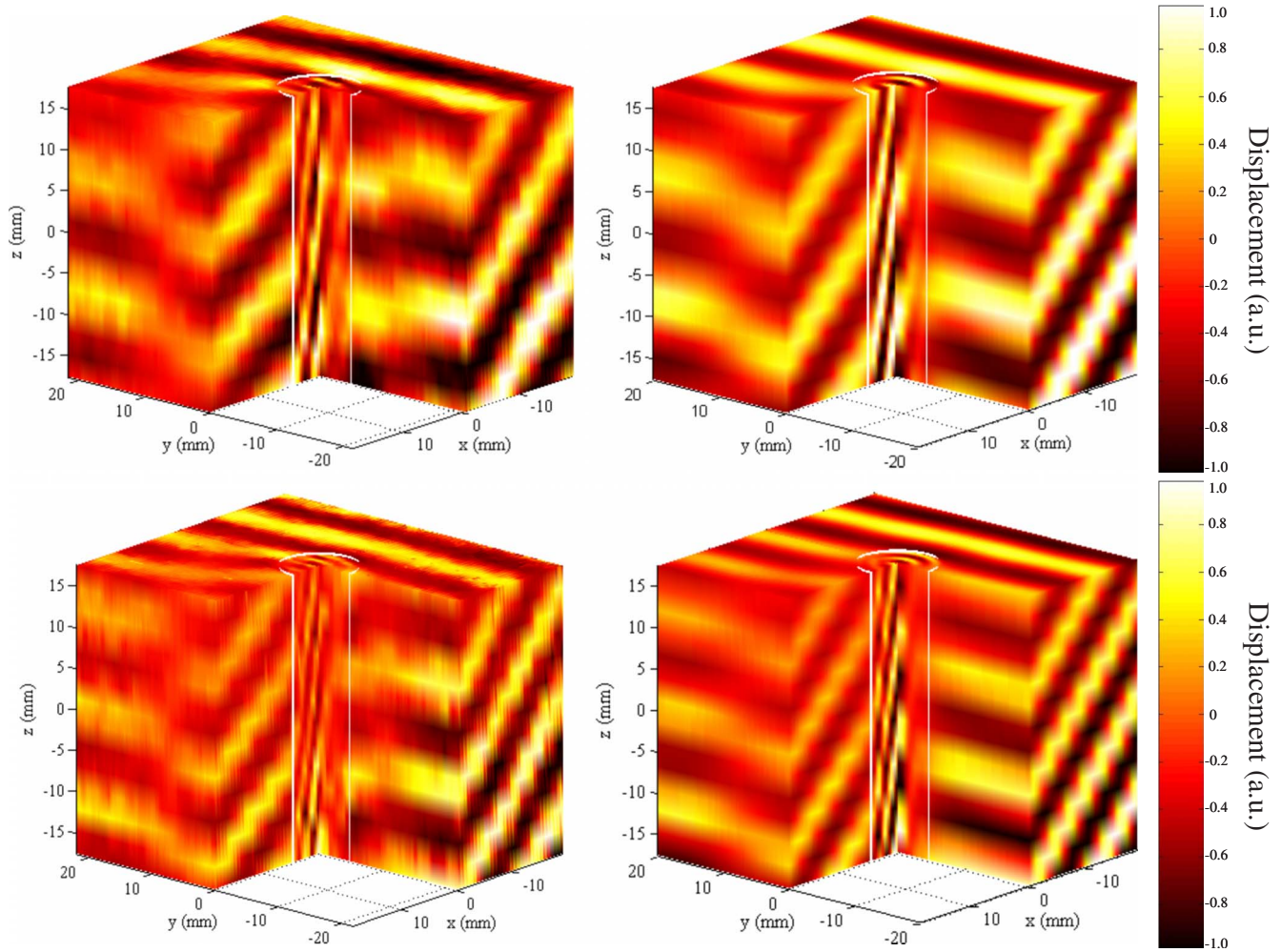

FIG. 4. (Color online) 3D representation of experimental (left) and simulated (right) normalized stationary displacement fields with $\alpha=46°$. The top and bottom images correspond to the scattering of 350 and 450 Hz harmonic incident waves, respectively.

ity and attenuation along 80 lines (of 38 mm width) at different depths. Viscoelasticity mean values were $\mu=(14600+0.7i\omega)$ Pa and $\mu=(1150+0.035i\omega)$ Pa for the surrounding medium and inclusion, respectively. Relative experimental errors were equal to $\pm 2.4\%$ and $\pm 14.0\%$ for elasticity and viscosity, respectively.

IV. EXPERIMENTAL VALIDATION OF THE 3D MODELS

A. Monochromatic case

The first experimental validation consisted in comparing experimental and theoretical stationary displacement fields due to the scattering of a monochromatic incident SW. This validation is necessary since the harmonic simulation also served to model a transient incident wave scattering. In addition, monochromatic excitation of soft tissues is commonly used in magnetic resonance elastography and in Doppler sonoelastography. Two harmonic excitations, 350 and 450 Hz, have been chosen to verify the validity of the harmonic model. This choice has been made because a large bandwidth was covered by the transient wave experimentally generated (see Fig. 2).

Figure 4 presents a 3D view of experimental and theoretical normalized displacements for the two harmonic excitations. A quarter volume was cut out from the entire scanned (or calculated) space in order to better visualize the displacement field into the inclusion. As one can see, a great similarity is noted between displacements within the inclusion and those within the surrounding medium for the two incident waves. One can also notice that the correspondence between simulations and measurements is not satisfied everywhere in the 3D space. In particular, it appears that the experimental frontwaves are not always strictly planar and that phase and amplitude shifts exist in certain regions. In order to compare more rigorously simulations with experiments and study the differences, the stationary fields were compared, first, following a plane Π (namely, the plane $z=-17.5$ mm), then along a line (1D) parallel to the x axis and contained in the plane Π, and finally along the z axis (i.e., the cylinder axis).

Figure 5 shows the 2D normalized stationary displacement fields in the plane Π for the two harmonic incident waves. The horizontal striations (jitter errors) appearing in the experimental displacements correspond to the piezoelectric elements of the ultrasonic linear array. It is noticeable that measurements contain experimental noise due to the relatively small amplitude of displacements at high frequencies (at lower frequencies, strong displacement modulations do not appear within the inclusion). Despite the presence of noise, one can see the good agreement between measured and theoretically predicted fields. For this example, the ex-

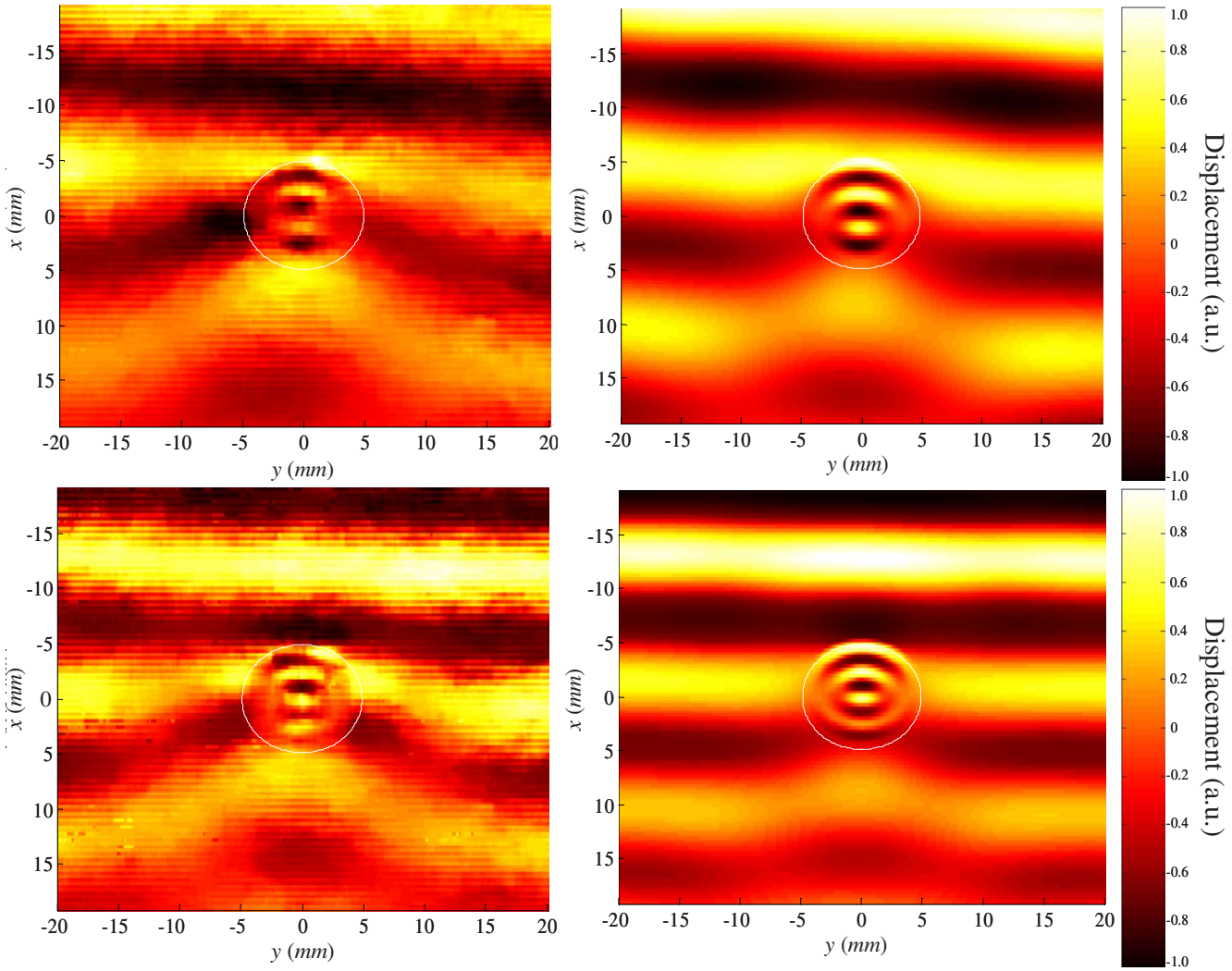

FIG. 5. (Color online) 2D representation of experimental (left) and simulated (right) normalized stationary displacement fields in the plane Π (corresponding to $z=-17.5$ mm). The top and bottom images correspond to the scattering of 350 and 450 Hz harmonic incident waves, respectively. The measured inclination β, in the plane $(o,\boldsymbol{e}_x,\boldsymbol{e}_y)$, equals −3°.

perimental incident wave was inclined, in the plane $(o,\boldsymbol{e}_x,\boldsymbol{e}_y)$, by an angle $\beta=-3°$ relative to the x axis. Figure 5 shows that this inclination, which has been measured and entered into the model, is correctly simulated.

One can also observe in Fig. 5 that the presence of oscillations in the inclusion is well simulated by the model. This is confirmed in Fig. 6 that represents, for both selected frequencies, the superposition of the experimental and simu-

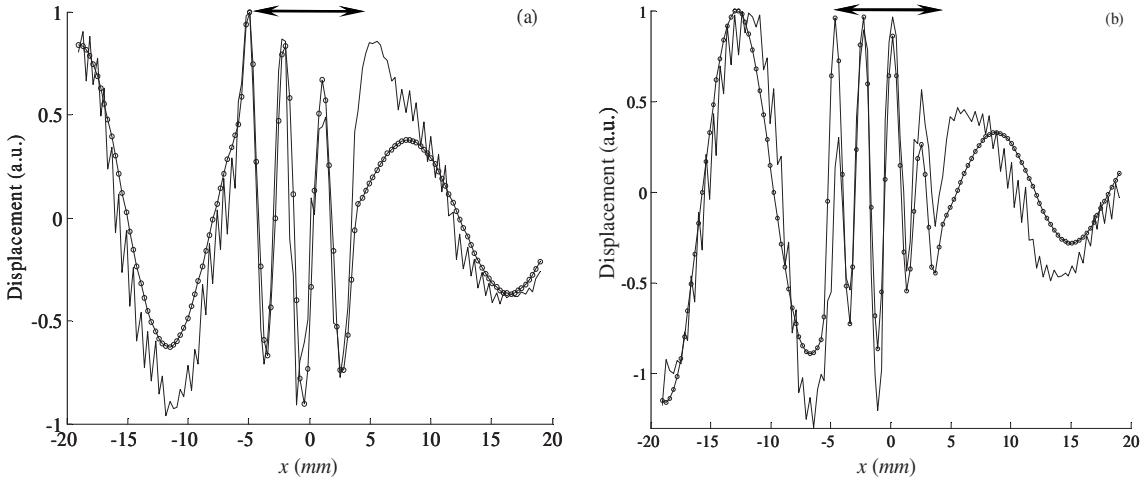

FIG. 6. Comparison of the experimental and simulated stationary displacements along the x axis in the plane Π for (a) a 350 Hz harmonic incident wave and (b) for a 450 Hz harmonic incident wave (— experimental; ⊖ simulation). The double arrow, in the top of figures, designates the inclusion spatial location.

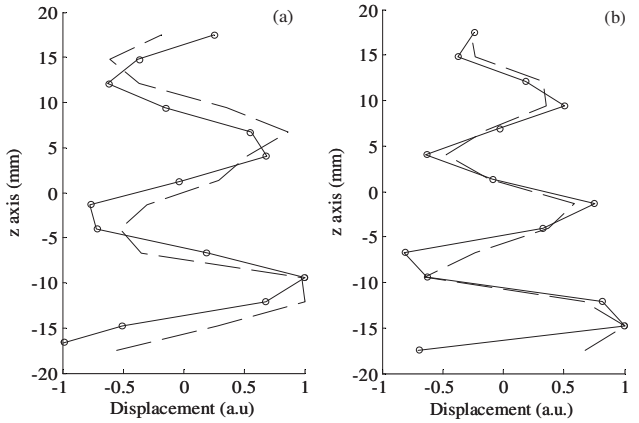

FIG. 7. Comparison of experimental and simulated stationary displacements along the z axis into the inclusion for (a) the 350 Hz harmonic incident wave and (b) for the 450 Hz harmonic incident wave (—— experimental; ⊖ simulation).

lated displacement profiles along a line ($y=0$) parallel to the x axis, crossing the inclusion and contained in the plane Π. A good correspondence between calculations and measurements is observable, except for the region immediately after the inclusion in the positive x direction. One can note the effect of attenuation increasing with frequency between the two plots, particularly in the region ranging between 5.0 and 20.0 mm. One may also notice differences in amplitude between measured and calculated displacements in Fig. 6 that are also observable in the stationary fields of Fig. 5. This is due to three principal reasons. The first one is the uncertainty in mechanical properties of materials composing inclusion and surrounding medium given in Sec. III B. Since theoretical displacements are calculated for mean values of the measured viscoelastic properties (which are global measurements), locally, slight differences between simulated and measured displacements (particularly for wave attenuation) can exist. The second source of differences is attributed to the relatively low spatial resolution in the lateral x direction because of the limited number of elements in the array transducer. The measured displacements were consequently subsampled (particularly into the inclusion where wavelengths are smallest) and an error on the inclusion localization occurred. Finally, the whole phantom dimensions were finite and the surrounding medium viscosity was relatively low. Experimentally, in the harmonic regime, this caused SW reflections at boundaries that perturbed the measured displacements into the inclusion and in its neighboring region.

The abovementioned sources of errors were simultaneously present but they did not dramatically affect the quality of measurements. This is also verified in Fig. 7, where experimental and theoretical stationary displacements along the z axis are compared for each tested frequency. As one can expect, the wavelength following the z direction, as in the other directions, is inversely proportional to the incident wave frequency (which is 14.5 and 11.3 mm at 350 and 450 Hz, respectively). The best agreement is thus noticed at the highest frequency of 450 Hz in Fig. 7. Existing differences could be explained by the spatial discretization error ($\Delta z = 2.5$ mm) and by elastic wave reflections at phantom boundaries that are strongest at low frequencies (since SWs are less attenuated at low frequencies).

Before concluding for the monochromatic case, it is important to point out that the presence of oscillations in the inclusion, observed in the horizontal planes (see, for example, Fig. 6) and along the vertical direction (as in Fig. 7), is directly related to the inclusion constitutive material viscoelasticity. Indeed, on one hand oscillation wavelengths are a function of elasticity, and on the other hand their amplitudes depend on both elasticity and viscosity. Another scattered wave characteristic is its spatial distribution in a given horizontal plane, i.e., the SW slowing down after crossing the inclusion, the orientation of diffraction lobes in the surrounding medium (see Fig. 5), the 2D shape of oscillations into the inclusion, the wave diffraction angle into the inclusion with respect to its axis, etc. All these behaviors are related to the internal and external viscoelastic properties and also to the contrast between them. Consequently, as it is developed in Sec. IV B, one could exploit this rich information to characterize mechanical properties of heterogeneous media.

B. Transient case

The harmonic 3D model is now used to simulate scattering of a transient SW with the previously described strategy. Both simulated and experimental incident waves were constituted by six oscillations, modulated by a Blackman temporal window to minimize Gibbs effects, with 350 Hz central frequency (see Fig. 2). Theoretical displacements are compared as a function of time with measurements obtained on the same phantom as the one used for the monochromatic excitation.

Figure 8 shows the transient wave propagation at different moments in half of the total 3D probed volume. This 3D view has been chosen to visualize more precisely the internal interaction of the incident SW with the cylindrical inclusion and the wave diffraction angle within the cylinder relative to the z axis. Time-varying experimental and simulated displacements are in good agreement in both inclusion and surrounding media. However, some comments can be made on the scattering behavior. First, it is noticeable that the experimental incident wave is not perfectly plane (this is observed at $t=21.8$ ms in the lower left part of the image). This explains slight differences between measured and predicted displacement fields. A second remark concerns oscillations observable in simulations in both inclusion and surrounding media before the incident wave arrival (see the right panel of Fig. 8 at $t=11.4$ ms). These artifacts are due to the Gibbs phenomenon, which appears when the scattering spectral solution is inversely Fourier transformed to the time domain. Indeed, since the scattering problem is solved for a finite frequency range, we applied the zero-padding technique outside this range to get the total spectral response. This numerical technique introduced a small discontinuity in the spectra and, in consequence, small nonphysical oscillations in the time response.

Despite these sources of errors, in addition to those referenced for the harmonic case (except reflections which are

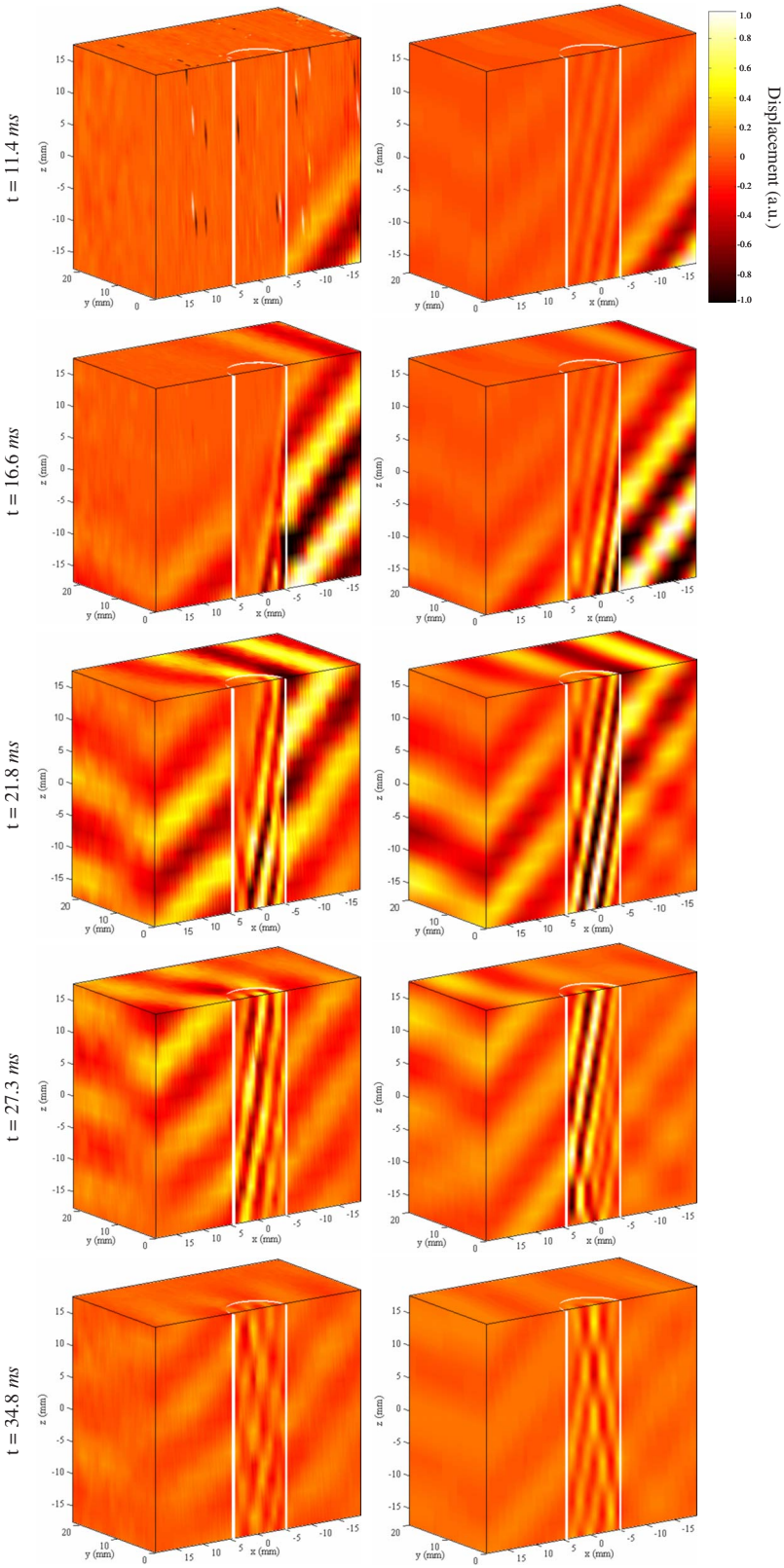

FIG. 8. (Color online) Time-varying 3D representation of the transient wave excitation scattered by the soft cylindrical inclusion. The view represents the half of the volume to visualize the behavior of the wave into the inclusion during the propagation. Inclination and incidence angles, β and α, were equal to $-3°$ and $46°$, respectively.

absent in the transient case), we can observe that the 3D transient SW scattering was well simulated by the model. It is important to notice that, as for the harmonic scattering problem, the wave distribution and amplitude are related to the medium viscoelasticity along the propagation path. Typically, the wavelength and the wave diffraction angle into the cylinder are related to the inclusion mechanical properties and to the contrast in viscoelasticity between both media, respectively.

V. CONCLUSION AND PERSPECTIVES

An analytical model was developed to simulate the scattering of an arbitrary (monochromatic or transient) plane SW by a circular cylindrical heterogeneity. Both inclusion and surrounding media constitutive materials were soft enough to allow the slow propagation of SWs which could, consequently, be imaged by an ultrafast ultrasonic system. The model validation was achieved experimentally on a heterogeneous phantom containing a very soft cylindrical inclusion. The comparison of measured and calculated 3D, 2D, and 1D stationary displacement fields has shown the model validity to simulate SW scattering by a cylindrical heterogeneity. The validated model then served to simulate the scattering of a transient plane SW (using the superposition principle). In this configuration, 3D theoretical temporal displacements were also in good agreement with measurements. When the geometrical and mechanical configurations of a scattering problem allow an analytical solving, analytical approaches are generally more precise, more stable, and faster than numerical methods (such as finite-element and finite-difference methods, well adapted to irregular scattering configurations). Moreover, analytical models allow the calculation of mechanical fields, such as displacement, strain, and stress, at any spatial position (a part of the plane, a line, or a set of points), without calculating in the whole volume like in numerical approaches. These advantages could be interesting to solve inverse problems using simulations.

In the context of dynamic elastography of soft structures, and more generally of living tissues, the approach developed in the present work could likely be applied to assess viscoelastic properties of venous blood clots, as introduced earlier. Indeed, these latter have a cylindrical shape (almost circular) and are constituted by coagulated blood with elasticity that does not exceed few kilopascals and a viscosity that is generally high.[5] Clot mechanical properties depend on several factors such as hematocrit level, the time elapsed since its formation in a blood vessel, chemical and metabolic conditions, etc. One can then consider to formulate and solve an inverse problem, into a strategy using both *in vivo* and simulated data, to perform mechanical property assessments of clots. The correlation of the assessed viscoelasticity with the clot age, its compactness, and biological constitution would provide to clinicians a complementary tool for venous thrombosis diagnosis and therapy planning. Moreover, the general 3D configuration considered here is compatible with real clinical conditions where mechanical excitation and ultrasound imaging angles can be arbitrary due, for example, to anatomical restrictions. The formulation and resolution of such inverse problem should deserve attention. Parallel to this direct application of the present work, the model could be developed to simulate scattering of SWs by a multilayer cylindrical inclusion. This extension would permit to treat the more general and realistic case of an inhomogeneous inclusion. To be more realistic, another avenue of development would be the simulation of SW interaction with geometrically and mechanically more complex heterogeneities (e.g., hollowed heterogeneities, elliptical cylinders, finite heterogeneities, anisotropic materials, etc.).

To conclude, this study showed that it is possible to analytically model SW interactions with soft bodies. The impact of this model is not limited to ultrasound elastography (in both harmonic and transient regimes) but also to MRI based elastography (monochromatic regime) that can be formulated in a similar framework. It is finally conceivable to extend this modeling strategy to other pathologies such as breast, brain, prostate and liver tumors, atherosclerosis, etc.

ACKNOWLEDGMENTS

This work was supported by a grant from the Canadian Institutes of Health Research (No. MOP-84358), by a National Scientist award of the Fonds de la Recherche en Santé du Québec (G.C.), and by postdoctoral (A.H.H.) and doctoral (C.S.) partial scholarships of the Groupe de Recherche en Sciences et Technologies Biomédicales of the Institute of Biomedical Engineering of the École Polytechnique and Université de Montréal.

Appendix

The (6×6) $\mathbf{T}_n$ matrix elements in Eq. (8) are given by

$$\mathbf{T}_n(1,1)=\frac{1}{2}K_1[J_{n-1}(K_1R)-J_{n+1}(K_1R)],\quad \mathbf{T}_n(1,2)=\frac{R}{2}k_1ik_{2_z}[J_{n-1}(k_1R)-J_{n+1}(k_1R)],$$

$$\mathbf{T}_n(1,3)=-\frac{n}{R}J_n(k_1R),\quad \mathbf{T}_n(1,4)=-\frac{1}{2}K_{2_\perp}[H_{n-1}^{(1)}(K_{2_\perp}R)-H_{n+1}^{(1)}(K_{2_\perp}R)],$$

$$\mathbf{T}_n(1,5)=-\frac{R}{2}k_{2_\perp}ik_{2_z}[H_{n-1}^{(1)}(k_{2_\perp}R)-H_{n+1}^{(1)}(k_{2_\perp}R)],\quad \mathbf{T}_n(1,6)=\frac{n}{R}H_n^{(1)}(k_{2_\perp}R),$$

$$\mathbf{T}_n(2,1)=\frac{n}{R}J_n(K_1R),\quad \mathbf{T}_n(2,2)=nik_{2_z}J_n(k_1R),\quad \mathbf{T}_n(2,3)=-\frac{1}{2}k_1[J_{n-1}(k_1R)-J_{n+1}(k_1R)],$$

$$\mathbf{T}_n(2,4)=-\frac{n}{R}H_n^{(1)}(K_{2_\perp}R),\quad \mathbf{T}_n(2,5)=-nik_{2_z}\times H_n^{(1)}(k_{2_\perp}R),$$

$$\mathbf{T}_n(2,6)=\frac{1}{2}k_{2_\perp}[H_{n-1}^{(1)}(k_{2_\perp}R)-H_{n+1}^{(1)}(k_{2_\perp}R)],$$

$$\mathbf{T}_n(3,1)=ik_{2_z}J_n(K_1R),$$

$$\mathbf{T}_n(3,2) = R\Bigg[-\frac{(k_1)^2}{4}(J_{n-2}(k_1R) - 2J_n(k_1R) + J_{n+2}(k_1R)) - \frac{k_1}{2R}(J_{n-1}(k_1R) - J_{n+1}(k_1R)) + \frac{n^2}{R^2}J_n(k_1R)\Bigg],$$

$$\mathbf{T}_n(3,3) = 0, \quad \mathbf{T}_n(3,4) = -ik_{2_z}H_n^{(1)}(K_{2_\perp}R),$$

$$\mathbf{T}_n(3,5) = R\Bigg[+\frac{(k_{2_\perp})^2}{4}(H_{n-2}^{(1)}(k_{2_\perp}R) - 2H_n^{(1)}(k_{2_\perp}R) + H_{n+2}^{(1)}(k_{2_\perp}R)) + \frac{k_{2_\perp}}{2R}(H_{n-1}^{(1)}(k_{2_\perp}R) - H_{n+1}^{(1)}(k_{2_\perp}R)) - \frac{n^2}{R^2}H_n^{(1)}(k_{2_\perp}R)\Bigg],$$

$$\mathbf{T}_n(3,6) = 0,$$

$$\mathbf{T}_n(4,1) = (\lambda_1 + 2\mu_1)\frac{(K_1)^2}{4}[J_{n-2}(K_1R) - 2J_n(K_1R) + J_{n+2}(K_1R)] - \lambda_1\left(\frac{n^2}{R^2} + (k_{2_z})^2\right)J_n(K_1R) + \lambda_1\frac{K_1}{2R}[J_{n-1}(K_1R) - J_{n+1}(K_1R)],$$

$$\mathbf{T}_n(4,2) = 2\mu_1\frac{R}{4}i(k_1)^2k_{2_z}[J_{n-2}(k_1R) - 2J_n(k_1R) + J_{n+2}(k_1R)] + 2\lambda_1\frac{1}{R}ik_{2_z}n^2J_n(k_1R),$$

$$\mathbf{T}_n(4,3) = +2\mu_1\frac{n}{R^2}J_n(k_1R) - \mu_1\frac{n}{R}k_1[J_{n-1}(k_1R) - J_{n+1}(k_1R)],$$

$$\mathbf{T}_n(4,4) = -(\lambda_2 + 2\mu_2)\frac{(K_{2_\perp})^2}{4}[H_{n-2}^{(1)}(K_{2_\perp}R) - 2H_n^{(1)}(K_{2_\perp}R) + H_{n+2}^{(1)}(K_{2_\perp}R)] + \lambda_2\left(\frac{n^2}{R^2} + (k_{2_z})^2\right)H_n^{(1)}(K_{2_\perp}R) - \lambda_2\frac{K_{2_\perp}}{2R}[H_{n-1}^{(1)}(K_{2_\perp}R) - H_{n+1}^{(1)}(K_{2_\perp}R)],$$

$$\mathbf{T}_n(4,5) = -2\mu_2\frac{R}{4}i(k_{2_\perp})^2k_{2_z}[H_{n-2}^{(1)}(k_{2_\perp}R) - 2H_n^{(1)}(k_{2_\perp}R) + H_{n+2}^{(1)}(k_{2_\perp}R)] - 2\lambda_2\frac{1}{R}ik_{2_z}n^2H_n^{(1)}(k_{2_\perp}R),$$

$$\mathbf{T}_n(4,6) = -2\mu_2\frac{n}{R^2}H_n^{(1)}(k_{2_\perp}R) + \mu_2\frac{n}{R}k_{2_\perp}[H_{n-1}^{(1)}(k_{2_\perp}R) - H_{n+1}^{(1)}(k_{2_\perp}R)],$$

$$\mathbf{T}_n(5,1) = -2\mu_1\frac{n}{R^2}J_n(K_1R) + \mu_1\frac{n}{R}K_1[J_{n-1}(K_1R) - J_{n+1}(K_1R)],$$

$$\mathbf{T}_n(5,2) = -2\mu_1\frac{n}{R}ik_{2_z}J_n(k_1R) + \mu_1ink_{2_z}k_1[J_{n-1}(k_1R) - J_{n+1}(k_1R)],$$

$$\mathbf{T}_n(5,3) = -\mu_1\frac{(k_1)^2}{4}[J_{n-2}(k_1R) - 2J_n(k_1R) + J_{n+2}(k_1R)] - \mu_1\frac{n^2}{R^2}J_n(k_1R) + \mu_1\frac{k_1}{2R}[J_{n-1}(k_1R) - J_{n+1}(k_1R)],$$

$$\mathbf{T}_n(5,4) = +2\mu_2\frac{n}{R^2}H_n^{(1)}(K_{2_\perp}R) - \mu_2\frac{n}{R}K_{2_\perp}[H_{n-1}^{(1)}(K_{2_\perp}R) - H_{n+1}^{(1)}(K_{2_\perp}R)],$$

$$\mathbf{T}_n(5,5) = +2\mu_2\frac{n}{R}ik_{2_z}H_n^{(1)}(k_{2_\perp}R) - \mu_2ink_{2_z}k_{2_\perp} \times[H_{n-1}^{(1)}(k_{2_\perp}R) - H_{n+1}^{(1)}(k_{2_\perp}R)],$$

$$\mathbf{T}_n(5,6) = +\mu_2\frac{(k_{2_\perp})^2}{4}[H_{n-2}^{(1)}(k_{2_\perp}R) - 2H_n^{(1)}(k_{2_\perp}R) + H_{n+2}^{(1)}(k_{2_\perp}R)] + \mu_2\frac{n^2}{R^2}H_n^{(1)}(k_{2_\perp}R) - \mu_2\frac{k_{2_\perp}}{2R} \times[H_{n-1}^{(1)}(k_{2_\perp}R) - H_{n+1}^{(1)}(k_{2_\perp}R)],$$

$$\mathbf{T}_n(6,1) = +2\mu_1ik_{2_z}K_1[J_{n-1}(K_1R) - J_{n+1}(K_1R)],$$

$$\mathbf{T}_n(6,2) = -\mu_1Rk_1(k_{2_z})^2[J_{n-1}(k_1R) - J_{n+1}(k_1R)] - \mu_1R\frac{(k_1)^2}{4}[J_{n-3}(k_1R) - 3J_{n-1}(k_1R) + 3J_{n+1}(k_1R) - J_{n+3}(k_1R)] + \mu_1\frac{k_1}{R}[J_{n-1}(k_1R) - J_{n+1}(k_1R)] - \mu_1\frac{(k_1)^2}{2}[J_{n-2}(k_1R) - 2J_n(k_1R) + J_{n+2}(k_1R)] - 4\mu_1\frac{n^2}{R^2}J_n(k_1R) + \mu_1\frac{n^2}{R}k_1[J_{n-1}(k_1R) - J_{n+1}(k_1R)],$$

$$\mathbf{T}_n(6,3) = -2\mu_1\frac{n}{R}ik_{2_z}J_n(k_1R),$$

$$\mathbf{T}_n(6,4) = -2\mu_2ik_{2_z}K_{2_\perp}[H_{n-1}^{(1)}(K_{2_\perp}R) - H_{n+1}^{(1)}(K_{2_\perp}R)],$$

$$\mathbf{T}_n(6,5) = +\mu_2 R k_{2_\perp}(k_{2_z})^2[H_{n-1}^{(1)}(k_{2_\perp}R) - H_{n+1}^{(1)}(k_{2_\perp}R)]$$
$$+\mu_2 R\frac{(k_{2_\perp})^2}{4}[H_{n-3}^{(1)}(k_{2_\perp}R) - 3H_{n-1}^{(1)}(k_{2_\perp}R)$$
$$+3H_{n+1}^{(1)}(k_{2_\perp}R) - H_{n+3}^{(1)}(k_{2_\perp}R)] - \mu_2\frac{k_{2_\perp}}{R}$$
$$\times[H_{n-1}^{(1)}(k_{2_\perp}R) - H_{n+1}^{(1)}(k_{2_\perp}R)] + \mu_2\frac{(k_{2_\perp})^2}{2}$$
$$\times[H_{n-2}^{(1)}(k_{2_\perp}R) - 2H_n^{(1)}(k_{2_\perp}R) + H_{n+2}^{(1)}(k_{2_\perp}R)]$$
$$+4\mu_2\frac{n^2}{R^2}H_n^{(1)}(k_{2_\perp}R) - \mu_2\frac{n^2}{R}k_{2_\perp}[H_{n-1}^{(1)}(k_2R)$$
$$-H_{n+1}^{(1)}(k_2R)],$$

$$\mathbf{T}_n(6,6) = +2\mu_2\frac{n}{R}ik_{2_z}H_n^{(1)}(k_{2_\perp}R).$$

The second member vector in Eq. (8) contains the nth components of displacement and stress due to the incident wave at the cylinder boundary. The $\mathbf{b}_n$ vector elements are as follows:

$$(b_1)_n = -\frac{\mathrm{amp}(\omega)}{\psi_0}\frac{n}{R}\varepsilon_n(i)^n J_n(k_{2_\perp}R),$$

$$(b_2)_n = -\frac{\mathrm{amp}(\omega)}{\psi_0}\frac{1}{2}k_{2_\perp}\varepsilon_n(i)^n[J_{n-1}(k_{2_\perp}R) - J_{n+1}(k_{2_\perp}R)],$$

$$(b_3)_n = 0,$$

$$(b_4)_n = \frac{\mathrm{amp}(\omega)}{\psi_0}2\mu_2\frac{n}{R^2}\varepsilon_n(i)^n J_n(k_{2_\perp}R)$$
$$-\frac{\mathrm{amp}(\omega)}{\psi_0}\mu_2\frac{nk_{2_\perp}}{R}\varepsilon_n(i)^n[J_{n-1}(k_{2_\perp}r) - J_{n+1}(k_{2_\perp}r)],$$

$$(b_5)_n = -\frac{\mathrm{amp}(\omega)}{\psi_0}\mu_2\frac{(k_{2_\perp})^2}{4}\varepsilon_n(i)^n[J_{n-2}(k_{2_\perp}R) - 2J_n(k_{2_\perp}R)$$
$$+J_{n+2}(k_{2_\perp}R)] + \frac{\mathrm{amp}(\omega)}{\psi_0}\mu_2\frac{k_{2_\perp}}{2R}\varepsilon_n(i)^n[J_{n-1}(k_{2_\perp}R)$$
$$-J_{n+1}(k_{2_\perp}R)] - \frac{\mathrm{Amp}(\omega)}{\psi_0}\mu_2\frac{n^2}{R^2}\varepsilon_n(i)^n J_n(k_{2_\perp}R),$$

$$(b_6)_n = -\frac{\mathrm{amp}(\omega)}{\psi_0}2\mu_2\frac{n}{R}\varepsilon_n(i)^{n+1}k_{2_z}J_n(k_{2_\perp}R).$$

[1]World Health Organization, http://www.who.int (Last viewed December 12, 2007).
[2]J. Hirsh and J. Hoak, "Management of deep vein thrombosis and pulmonary embolism: A statement for healthcare professionals from the Council on thrombosis (in consultation with the council on cardiovascular radiology)," Circulation **93**, 2212–2245 (1996).
[3]M. Kaibara, "Rheology of blood coagulation," Biorheology **33**, 101–117 (1996).
[4]J. V. Shah and P. A. Janmey, "Strain hardening of fibrin gels and plasma clots," Rheol. Acta **36**, 262–268 (1997).
[5]J.-L. Gennisson, S. Lerouge, and G. Cloutier, "Assessment by transient elastography of the viscoelastic properties of blood during clotting," Ultrasound Med. Biol. **32**, 1529–1537 (2006).
[6]S. Y. Emelianov, X. Chen, M. O'Donnell, B. Knipp, D. Myers, T. W. Wakefield, and J. M. Rubin, "Triplex ultrasound: Elasticity imaging to age deep venous thrombosis," Ultrasound Med. Biol. **28**, 757–767 (2002).
[7]J. M. Rubin, S. R. Aglyamov, T. W. Wakefield, M. O'Donnell, and S. Y. Emelianov, "Clinical application of sonographic elasticity imaging for aging of deep venous thrombosis: Preliminary findings," J. Ultrasound Med. **22**, 443–448 (2003).
[8]R. M. Lerner, K. J. Parker, J. Holen, R. Gramiak, and R. C. Waag, "Sonoelasticity: Medical elasticity images derived from ultrasound signals in mechanically vibrated targets," Acoust. Imaging **16**, 317–327 (1988).
[9]Y. Yamakoshi, J. Sato, and T. Sato, "Ultrasonic imaging of internal vibration of soft tissue under forced vibration," IEEE Trans. Ultrason. Ferroelectr. Freq. Control **37**, 45–53 (1990).
[10]A. Eisencher, E. Schweg-Toffler, G. Pelletier, and P. Jacquemard, "La palpation échographique rythmée: Echosismographie," J. Radiol. **64**, 255–261 (1983).
[11]T. A. Krouskop, D. R. Dougherty, and F. S. Vinson, "A pulsed Doppler ultrasonic system for making noninvasive measurements of the mechanical properties of soft tissue," J. Rehabil. Res. Dev. **24**, 1–8 (1987).
[12]K. J. Parker and R. M. Lerner, "Sonoelasticity of organs: Shear waves ring a bell," J. Ultrasound Med. **11**, 387–392 (1992).
[13]R. Muthupillai, D. J. Lomas, P. J. Rossman, J. F. Greenleaf, A. Manduca, and R. L. Ehman, "Magnetic resonance elastography by direct visualization of propagating acoustic strain waves," Science **269**, 1854–1857 (1995).
[14]S. Catheline, F. Wu, and M. Fink, "A solution to diffraction biases in sonoelasticity: The acoustic impulse technique," J. Acoust. Soc. Am. **105**, 2941–2950 (1999).
[15]L. Sandrin, M. Tanter, S. Catheline, and M. Fink, "Shear modulus imaging with 2D transient elastography," IEEE Trans. Ultrason. Ferroelectr. Freq. Control **49**, 426–435 (2002).
[16]J. Bercoff, M. Tanter, and M. Fink, "Supersonic shear imaging: A new technique for soft tissue elasticity mapping," IEEE Trans. Ultrason. Ferroelectr. Freq. Control **51**, 396–409 (2004).
[17]M. L. Palmeri, A. C. Sharma, R. R. Bouchard, R. W. Nightingale, and K. R. Nightingale, "A finite-element method model of soft tissue response to impulsive acoustic radiation force," IEEE Trans. Ultrason. Ferroelectr. Freq. Control **52**, 1699–1712 (2005).
[18]J. J. Faran, "Sound scattering by solid cylinders and spheres," J. Acoust. Soc. Am. **23**, 405–418 (1951).
[19]R. M. White, "Elastic wave scattering at a cylindrical discontinuity in a solid," J. Acoust. Soc. Am. **30**, 771–785 (1958).
[20]Y. Fan, A. N. Sinclair, and F. Honarvar, "Scattering of a plane acoustic wave from a transversely isotropic cylinder encased in a solid elastic medium," J. Acoust. Soc. Am. **106**, 1229–1236 (1999).
[21]F. Honarvar and A. N. Sinclair, "Acoustic wave scattering from transversely isotropic cylinders," J. Acoust. Soc. Am. **100**, 57–63 (1996).
[22]S. Catheline, J.-L. Gennisson, G. Delon, M. Fink, R. Sinkus, S. Abouelkaram, and J. Culioli, "Measurement of viscoelastic properties of homogeneous soft solid using transient elastography: An inverse problem approach," J. Acoust. Soc. Am. **116**, 3734–3741 (2004).
[23]C. Schmitt, A. Hadj Henni, and G. Cloutier, "Characterization of time-varying mechanical viscoelastic parameters of mimicking deep vein thrombi with 2D dynamic elastography," in IEEE International Ultrasonics Symposium, New York (2007), pp. 28–31.
[24]J. D. Achenbach, *Wave Propagation in Elastic Solids* (North-Holland, Amsterdam, 1973).
[25]P. M. Morse and H. Feshbach, *Methods of Theoretical Physics* (McGraw-Hill, New York, 1953).
[26]Matlabs® User's Guide, Mathworks, Inc., Natick, MA, http://www.mathworks.com
[27]E. Chérin, R. Williams, A. Needles, G. Liu, C. White, A. S. Brown, Y.-Q. Zhou, and F. S. Foster, "Ultrafast frame rate retrospective ultrasound microimaging and blood flow visualization in mice *in vivo*," Ultrasound Med. Biol. **32**, 683–691 (2006).
[28]M. Pernot, K. Fujikura, S. D. Fung-Kee-Fung, and E. Konofagou, "ECG-gated, mechanical and electromechanical wave imaging of cardiovascular tissues *in vivo*," Ultrasound Med. Biol. **33**, 1075–1085 (2007).
[29]J.-L. Gennisson and G. Cloutier, "Sol-Gel transition in agar-gelatin mixtures studied with transient elastography," IEEE Trans. Ultrason. Ferroelectr. Freq. Control **53**, 716–723 (2006).